Optimizing Low-Complexity Analog Mappings for Low-Power Sensors with Energy Scheduling Capabilities

Boules A. Mouris, *Student Member, IEEE,* Photios A. Stavrou, *Member, IEEE,* Ragnar Thobaben, *Member, IEEE,*

***Abstract*—ower consumption is a major challenge for massive deployment of wireless sensors in internet of things (IoT) networks. This paper studies the use of analog joint source-channel (AJSCC) mappings in low-power sensing schemes. In particular, we propose a novel *triangular* mapping geometry as a low-complexity dimension reduction mapping. The proposed triangular mapping is employed for analog compression of multiple sensor readings into one signal, and thus, limits the need for power-hungry analog-to-digital conversion and processing at the sensing nodes. A comprehensive performance analysis of the proposed triangular mapping in terms of the mean squared error (MSE) performance is provided analytically and verified numerically. The problem of mapping adaptation to different source distributions is also studied. Moreover, the proposed triangular mapping is adopted in an energy scheduling problem in which the sensing nodes schedule their use of the received powers at different time instants and adjust the mapping parameters accordingly with the goal of minimizing the sum distortion at the receiver. We present a fast low-complexity algorithm for optimal energy scheduling and verify its performance in comparison with commercial convex optimization solvers. It is shown that the proposed mapping provides a very good MSE performance compared to the AJSCC benchmarks despite having a much lower complexity circuit implementation.ower consumption is a major challenge for massive deployment of wireless sensors in internet of things (IoT) networks. This paper studies the use of analog joint source-channel (AJSCC) mappings in low-power sensing schemes. In particular, we propose a novel *triangular* mapping geometry as a low-complexity dimension reduction mapping. The proposed triangular mapping is employed for analog compression of multiple sensor readings into one signal, and thus, limits the need for power-hungry analog-to-digital conversion and processing at the sensing nodes. A comprehensive performance analysis of the proposed triangular mapping in terms of the mean squared error (MSE) performance is provided analytically and verified numerically. The problem of mapping adaptation to different source distributions is also studied. Moreover, the proposed triangular mapping is adopted in an energy scheduling problem in which the sensing nodes schedule their use of the received powers at different time instants and adjust the mapping parameters accordingly with the goal of minimizing the sum distortion at the receiver. We present a fast low-complexity algorithm for optimal energy scheduling and verify its performance in comparison with commercial convex optimization solvers. It is shown that the proposed mapping provides a very good MSE performance compared to the AJSCC benchmarks despite having a much lower complexity circuit implementation.P**

***Index Terms*—joint source-channel coding, analog mappings, energy harvesting, low-power sensors.**

The authors are with the Division of Information Science and Engineering (ISE), School of Electrical Engineering and Computer Science, KTH Royal Institute of Technology, Stockholm, Sweden (e-mail: boules@ieee.org).

I. Introduction

WIRELESS sensors form an important building block of the Internet of Things (IoT). In fifth-generation (5G) IoT networks, the bottom physical layer is dedicated to wireless sensors and is referred to as the sensor layer [1]. They are widely viewed as the bridge between the physical world and the cyber world [2]. IoT relies on wireless sensors in numerous real-world applications such as environmental monitoring, healthcare, smart transportation, and smart agriculture [1]. In these applications, wireless sensors are expected to enable smart monitoring and control while minimizing human interaction. With the IoT growing and sensors being installed at massive rates, the need for self-sustainable IoT sensors has drastically increased. Limiting human interaction is of particular importance in order to maintain sustainability and minimize the maintenance costs on one hand. On the other hand, some applications may involve sensors deployed in an unreachable or hazardous environment; for example, implants in human bodies, chemical reactors, extreme weather conditions, or providing emergency response to disasters [3].

Battery usage remains as the major issue facing self-sustainable IoT sensors. Consequently, giving rise to the question whether it is possible to power these sensors without the need for conventional battery recharging/replacement or not. An appealing possibility is to rely on energy harvesting from ambient sources such as solar, vibrational, thermal and electromagnetic energy. However, ambient energy harvesting depends on the environment and does not provide control of the amount of energy delivered to the sensors [4]. Controlling the amount of available energy at the sensor node becomes of great importance in critical data transmission where availability needs to be guaranteed, like in health care applications or industrial control applications (e.g., industry 4.0). For this reason, wireless power transfer (WPT) has emerged as a promising controllable alternative to ambient energy harvesting. In WPT, a dedicated power transmitter is used to send RF power to the energy harvester with the goal of guaranteeing a minimum amount of energy transfer. The power transmitter could take the form of a multi-antenna base station [5], [6], unmanned aerial vehicle (UAV) [7]–[9], or an on-body access point [10], [11].

A. Related Work

In order to rely on WPT and energy harvesting for powering IoT sensors, an essential requirement is to minimize their

power consumption and to optimize their performance for a given energy budget as considered in this paper. Analog joint source-channel coding (AJSCC) has recently been proposed for minimizing the power consumption of IoT sensors by limiting the use of power-hungry analog-to-digital converters at the sensor nodes [12]–[17]. Within this framework, AJSCC is used to compress[1] the reading of two or more sensors into one signal and transmit it through the wireless channel through analog or hybrid analog-digital communication schemes.

Although the idea of AJSCC was introduced by Shannon more than seventy years ago [19], no practical implementation of AJSCC schemes has been presented in the literature until very recently. To the best of the authors' knowledge, [12] was the first work to propose a low-complexity implementation of AJSCC using analog circuit components. Prior to [12], AJSCC was only implemented using software-defined radios such as in [20]. Implementing AJSCC for image compression using neural networks has recently been presented in [21]. However, neither software-defined radio nor neural networks are suitable for implementation in a low-power sensing node. The use of AJSCC for compression in a low-power sensing node relies on low-complexity dimension reduction mappings similar to those in [22]. In such mappings, $N:1$ compression is performed by projecting the source point (sensor readings) into a space-filling curve (geometry) and then the length from the origin of the curve to the projected point is used as the encoded signal. So far, there is no general method to design the geometry of the dimension reduction mappings [18]. One method that is widely used in the literature is to analytically approximate the results obtained from power-constrained channel-optimized vector quantizers (PCCOVQ) [23], [24]. An example for this method is the Archimedean spiral mapping presented in [25] providing a performance close to the optimal mapping in the case of 2:1 compression of Gaussian sources (see [26]). The other approach relies on doing some sophisticated guess work to introduce a mapping geometry that can be described using an analytic function while covering the source space efficiently and minimizing the distortion error. Examples of such mappings can be found in [22]. The rectangular mapping studied in [12] and proposed for low-power sensors is another example of 2:1 mappings based on space-filling curves. It can be viewed as a refined version of the original one introduced by Shannon in [19]. The circuit implementation of the rectangular mapping introduced in [12] enabled more research on analyzing its performance [14], [15], improving the circuit implementation [13], and finding applications in wireless monitoring [16] and health care [15]. Moreover, inspired by the rectangular mapping, an alternative dimension reduction mapping based on MOSFET I-V characteristics has been proposed and studied in [16], [17].

Although the use of AJSCC in wireless sensors aims at exploiting energy harvesting as a source of power [12], [13], [16], no existing work has discussed the link between the harvested energy (the available power at the sensor node) and the performance of the mapping. Moreover, to the best of the authors' knowledge, no present work has investigated the use energy scheduling to optimize the mapping performance over time. Besides, the present literature on the use of AJSCC in IoT sensors lacks the explanation on how the low-complexity AJSCC mappings can exploit the different types of correlations between the sensor signals to improve the performance in terms of the distortion at the receiver node.

[1]It is worth mentioning that AJSCC can also be used for dimension expansion [18]. However, dimension reduction is more relevant in the context of this work and for low-power sensors.

B. Contributions

In this paper, we first propose a novel *triangular* mapping geometry as a low-complexity dimension reduction mapping inspired by the rectangular mapping presented in [12]. We provide a complete theoretical analysis of the proposed mapping and discuss its practical circuit implementation. We show that the proposed triangular mapping maintains the same mean squared error (MSE) performance as the rectangular mapping in the high signal-to-noise ratio (SNR) scenario while having a simpler circuit implementation. The proposed triangular mapping as well as the rectangular mapping can be considered to fill the gap of implementing low-complexity AJSCC mappings in low-power sensing schemes. Secondly, different methods to improve the performance of the proposed triangular mapping are presented. For example, by adapting the mapping to the source distribution and/or the different types of correlation existing between the source signals. To the best of the authors' knowledge, this is the first work to consider low-complexity implementable mapping adaptation methods. Finally, we study the problem of optimizing the AJSCC mapping according to the available harvested power at different time instants at the sensor node. We assume that each sensor node is equipped with a battery and is able to save power for later use. An energy scheduling problem is then formulated with the goal of choosing the optimal design parameters of the mapping to minimize the sum distortion at the receiver node. A fast low-complexity algorithm for optimal energy scheduling is proposed. The presented energy scheduling algorithm can be considered as the next step towards making it possible for the upcoming technologies to exploit AJSCC in wireless powered sensing schemes.

To summarize the above, the contributions of this paper can be listed as follows:

- We propose and study a *triangular* mapping as a novel low-complexity dimension reduction mapping. A theoretical analysis of the MSE performance of the proposed mapping is provided and verified numerically.
- We discuss the real world circuit implementation of the proposed triangular mapping showing significant advantages over a similar implementation that makes use of the rectangular mapping in terms of implementation complexity.
- We present different methods for improving the MSE performance of the mapping such as adapting the mapping to distribution of the input signals as well as exploiting different types of correlation between the source signals. We verify the performance improvement through simulations. In addition, practical implementation of these improvement methods is also discussed.

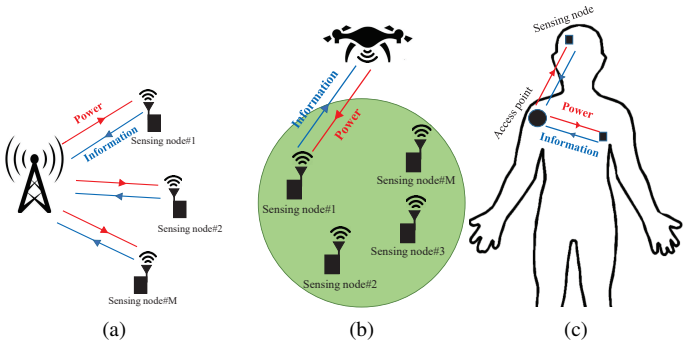

Fig. 1. Wirelessly powered sensors nodes communicating with (a) a base station, (b) a UAV, (c) an on-body access point.

- We formulate an energy scheduling problem to optimize the mapping parameters (i.e., its performance) according to energy arrivals at the sensing node in a wirelessly powered sensors scenario. We propose a fast low-complexity algorithm for optimal energy scheduling with the goal of minimizing the sum MSE. The performance of the proposed algorithm is verified in comparison with commercial convex optimization solvers. We show by simulations that the sum MSE can be significantly improved when energy scheduling capabilities are exploited compared to consuming the available energy instantly without scheduling.

C. Outline

The rest of the paper is organized as follows: The system model and the proposed triangular mapping are introduced in Section II. Section III discusses the performance and optimization of the proposed mapping. Section IV presents the different techniques to improve the MSE performance of the mapping according to the distribution of the input signals. The problem of optimal energy scheduling is studied in Section V. The simulations results are shown in Section VI. Conclusions and future work are discussed in Section VII.

Notation: Vectors are represented by bold lower case letters. Non-bold symbols represent scalars. The operator $|.|$ with a scalar argument represents the absolute value, with a vector argument represents the Euclidean norm. $\mathbf{x}^T$ refer to the transpose of a vector. $\mathbb{P}\{.\}$ and $\mathbb{E}\{.\}$ denote the probability and expectation operators, respectively. We let $\mathcal{N}\left(\mu, \sigma^2\right)$ be a Gaussian distribution with mean μ and variance σ^2. $\mathrm{U}\left[a, b\right]$ represents a uniform distribution in the interval $[a, b]$. $Q\left(\cdot\right)$ denotes the tail probability function of the standard Gaussian distribution.

II. System Model

A. Wirelessly Powered Sensor Network

In this paper, we are interested in the setup described in Fig. 1 representing a system of wireless sensors at fixed positions receiving power from a dedicated power transmitter such as a multi-antenna base station (Fig. 1a), a UAV (Fig. 1b), or an on-body access point (Fig. 1c). The transmitter in our considered setup serves as a hybrid access point (HAP) transmitting power and receiving information from the sensing node. Similar setups for wirelessly powered communication systems can be found in [7], [9], [11], [27]. We assume a system of M sensing nodes each containing N_s sensors connected together. Each sensing node is equipped with a battery, an energy harvester, and a single-antenna RF transmitter. The HAP is equipped with N_t antennas and operates as a power transmitter and an information receiver. We assume that different frequencies are allocated to power transmission and information reception to minimize interference. Although, in practice, the sensing nodes may have hybrid energy harvesting capabilities to harvest energy from other ambient sources as well (e.g., solar or vibrational energy) [4], in this work, we focus on controllable reception of power from the dedicated power transmitter in this work. The sensors use the received power to perform their measurements, compress their reading into one signal using AJSCC, then the compressed signal is sent from the sensing node to the HAP. The HAP sequentially repeats this process for all the sensing nodes until it collects the readings of the M nodes. Then, it starts from sensing node$\#1$ all over again.

B. Sensing Node

For simplicity, we assume at first that each sensing node consists of $N_s = 2$ sensors. The extension to the case where $N_s > 2$ is discussed in Appendix B. At each sensing node, the readings of the two sensors are combined together and compressed using a dimension reduction (2:1) mapping and sent through the channel. A block diagram describing the idea of dimension reduction is shown in Fig. 2. Here, the source signals (sensor readings) are denoted by $\mathbf{s} = [s_1\,,\, s_2]$. In our model, the sensor readings are assumed to be slowly varying continuous analog signals with s_1 following a marginal probability density function (PDF) p_1 bounded[2] within the range $[0, R_1]$. Similarly, s_2 follows a marginal PDF p_2 bounded within the range $[0, R_2]$. At each sensor node, a dimension reduction mapping (represented by an encoding function $f(\mathbf{s})$) is applied to compress the source signals into one signal x which is then used as input to the communication channel.

In this work, a *triangular* mapping is proposed as a simpler alternative to the rectangular space-filling curve which is introduced previously in the literature [12], [19]. The idea of triangular mapping is illustrated in Fig. 3. It consists of parallel lines all pointing towards the same direction. Here, dimension reduction is achieved by projecting the pair of source signals $(s_1,\ s_2)$ onto the curve by finding the closest point on the curve (as illustrated in Fig. 3). The projection is then represented using the aggregate length of the curve from the origin up to the mapped point (red lines in Fig. 3). The rectangular mapping discussed in [12], [19] also consists of parallel lines in a similar way to that shown in Fig. 3. However, different from the proposed triangular mapping, the direction of the parallel lines alternates at each level. Although the difference between the geometry of both mappings is small,

[2]For PDFs with infinite boundaries (e.g., Gaussian distribution), the tail of the PDF is truncated introducing some uncontrolled overload distortion. More discussion on overload discussion can be found in Sec. III-A. Furthermore, if the PDF extends to negative values, a simple translation of axis operation can be applied to shift the boundaries to the positive value range.

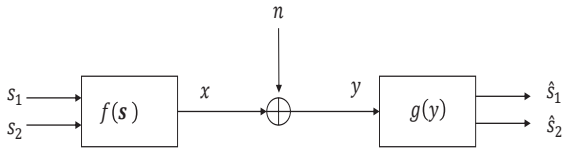

Fig. 2. Block diagram of the 2:1 dimension reduction mapping.

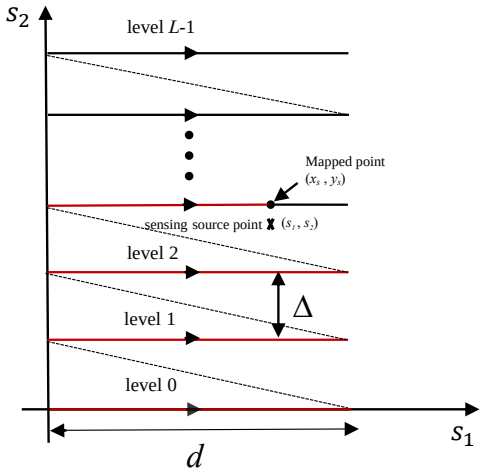

Fig. 3. The proposed triangular mapping.

the triangular mapping results in a much lower complexity circuit implementation as will be discussed later in this section.

In order to describe the encoding function analytically and analyze the triangular mapping's performance, we assume that the number of parallel lines (levels) in the y-axis is denoted by L and the length of each level in the x-axis is represented by d (corresponding to a certain voltage value). Let the maximum aggregate length of the mapping be described by $\gamma = Ld$. The value of γ can be viewed as the maximum voltage that can be obtained as an output of the triangular mapping due to a power or voltage constraint. It follows that the encoding function $f(\mathbf{s})$ for 2:1 dimension reduction using the proposed triangular mapping is expressed as

$$f_{\triangle}(\mathbf{s}) = d\left(k + \frac{s_1}{R_1}\right), \tag{1}$$

where $k = \text{round}(\frac{s_2}{\Delta})$ with Δ being the spacing between levels.

A block diagram describing the analog circuit implementation of the above encoding function is shown in Fig. 4. It consists of two branches whose outputs are added together using an analog adder to form the output of the AJSCC encoder. The first branch consists of a voltage divider that divides its input voltage of s_2 by a tunable voltage Δ and outputs the integer part of the division. The output of the voltage divider is then applied to an analog multiplier that multiplies it by a variable voltage d. The multiplier's output represents the output of the first branch. In the second branch, the voltage of s_1 is applied to a voltage-controlled voltage source (VCVS) whose output is directly proportional to its input with a tunable

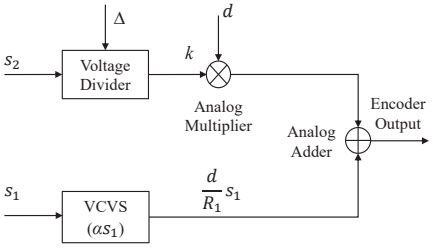

Fig. 4. Block diagram of the analog circuit implementation of the encoding function.

proportionality constant (i.e., αs_1). The output of the VCVS is taken as the output of the second branch. In order to highlight the differences from the rectangular mapping, we express the encoding function of the rectangular mapping using our notation as $f_{\square}(\mathbf{s}) = (1-\zeta)d\left(k + \frac{s_1}{R_1}\right) + \zeta d\left(k+1-\frac{s_1}{R_1}\right)$ with $\zeta = \text{mod}(k, 2)$. A key difference between the triangular mapping encoding function and that of the rectangular mapping, is that the latter requires two different types of VCVS (directly and inversely proportional to their inputs). Moreover, it requires an additional implementation of the modulo operation ($\text{mod}(k, 2)$) to select the VCVS corresponding to each level. Performing such modulo operation requires implementing a multi-stage analog divider [13, Sec. IV], and hence, increases complexity and power consumption. The advantages of the triangular mapping in terms of the lower complexity circuit implementation can be easily observed by comparing the block diagram in Fig. 4 to that of the rectangular mapping in [13, Fig. 5].

III. Performance and Optimization of the Baseline Mapping

In this section, we analyze the MSE performance of the proposed triangular mapping considering different SNR scenarios. Then, different methods to optimize the parameters of the mapping are discussed. For the analysis in this section, we assume that the source signals are uncorrelated. Certain types of correlation between the source signals will be taken into account in Sec. IV-B.

A. MSE performance of the proposed 2:1 triangular mapping

Applying the encoding function in (1) to the source point (s_1, s_2), the obtained mapped point (represented by the black dot in Fig. 3) on the triangular mapping is denoted by (x_s, y_s). Here, $x_s = \frac{d}{R_1}s_1$ is a scaled version of s_1 to fit the length of each level to the range R_1 and $y_s = k\Delta$ is the discretized version of s_2 with $\Delta = \frac{R_2}{L-1}$. The term y_s can alternatively be expressed as $y_s = s_2 + \lambda_y$, where λ_y is the quantization error term due to discretizing s_2. For a uniformly distributed source and a uniform quantizer with fixed spacing Δ [28, Ch. 5.4], the quantization error term λ_y is a uniformly distributed random variable in the range $\left[-\frac{\Delta}{2}, \frac{\Delta}{2}\right]$. It follows that

$$|\lambda_y| = \left|s_2 - \text{round}(\frac{s_2}{\Delta})\Delta\right|, \tag{2}$$

with $\mathbb{E}\left\{|\lambda_y|^2\right\} = \frac{\Delta^2}{12}$. This holds in good approximation even for other distributions for sufficiently small Δ [28, Ch. 5.4].

The encoded signal $x = f(\mathbf{s})$ is then transmitted through the channel. To decouple the analysis from the used modulation format, we consider the equivalent real-valued baseband model with an additive white Gaussian noise (AWGN) channel, i.e., $y = x+n$ with $n \sim \mathcal{N}\left(0, \sigma_n^2\right)$. Typically, for efficient wireless power transmission, a strong LOS link exists between the HAP and the sensor node [7], [29]. Therefore, it is reasonable to assume perfect channel state information (CSI) knowledge at the receiver (HAP) node. Following that assumption, matched filtering can be applied to convert the single input multiple output (SIMO) channel between the sensor node and the UAV to its equivalent scalar channel and treat it in a similar way to an AWGN channel [30]. At the receiver node, an estimator is applied to the received signal to recover the pair of source signals $(\hat{s}_1, \hat{s}_2) = g(y)$. We assume that the decoder performs the reverse mapping on the received signal using maximum likelihood (ML) estimation. The ML estimator is defined as

$$(\hat{s}_1, \hat{s}_2) = \underset{s_1, s_2}{\arg\max}\ \mathbb{P}\left(y | s_1, s_2\right). \tag{3}$$

The distortion at the receiver in terms of the MSE is expressed as

$$\mathrm{MSE} = \mathbb{E}\left\{|\hat{s}_1 - s_1|^2\right\} + E\left\{|\hat{s}_2 - s_2|^2\right\}. \tag{4}$$

Two sources of decoding error affect the MSE performance of the ML estimator. First, when the noise perturbates the received signal on the same level without stage crossing (no jumping to an upper or lower level). Second, if the noise term is large, stage crossing can occur in which the received signal may jump to a lower level or an upper level depending on the sign of the noise term. Jumping to the lower (higher) level is referred to as left (right) stage crossing. Therefore, the overall MSE expression in (4) can generally be decomposed into three quantities as follows

$$\mathrm{MSE} = \mathrm{MSE}_{\mathrm{mid}} + \mathrm{MSE}_{\mathrm{rc}} + \mathrm{MSE}_{\mathrm{lc}}, \tag{5}$$

where $\mathrm{MSE}_{\mathrm{mid}}$ is the MSE when no stage crossing exists (i.e., noise is not strong enough to jump from one level to the other). $\mathrm{MSE}_{\mathrm{rc}}$ is the MSE due to right stage crossing, and $\mathrm{MSE}_{\mathrm{lc}}$ is the MSE due to the left stage crossing.

When the condition $-\frac{d}{R_1}s_1 < n < d - \frac{d}{R_1}s_1$ is satisfied, the noise term perturbates the received signal on the same level without stage crossing. In such case, the received components of the signal are $x_r = x_s + n$, and $y_r = y_s$. The estimated signals using ML are given by $\hat{s}_1 = \frac{R_1}{d}x_r = \frac{R_1 L}{\gamma}(x_s + n) = s_1 + \frac{R_1 L}{\gamma}n$ and $\hat{s_2} = y_s = s_2 + \lambda_y$. Consequently, $\mathrm{MSE}_{\mathrm{mid}}$ can be expressed as

$$\mathrm{MSE}_{\mathrm{mid}} \quad = \quad \left(\frac{R_1^2 L^2}{\gamma^2}\mathbb{E}\left\{|n|^2\right\} + \mathbb{E}\left\{|\lambda_y|^2\right\}\right) p_m, \tag{6}$$

with $p_m = \mathbb{P}\left\{-\frac{d}{R_1}s_1 < n < d - \frac{d}{R_1}s_1\right\}$. The above expression can be written in terms of the mapping parameters as follows

$$\mathrm{MSE}_{\mathrm{mid}} = \left(\frac{R_1^2 L^2}{\gamma^2}\sigma_n^2 + \frac{1}{12}\frac{R_2^2}{(L-1)^2}\right) p_m, \tag{7}$$

where $p_m = 1 - \left(\mathbb{P}\left\{n > d - \frac{d}{R_1}s_1\right\} + \mathbb{P}\left\{n < -\frac{d}{R_1}s_1\right\}\right)$ and can be expressed as

$$p_m = 1 - \left(\int_0^{R_1} p_1(s_1)\ Q\left(\frac{d - \frac{d}{R_1}s_1}{\sigma_n}\right) ds_1 + \int_0^{R_1} p_1(s_1)\ Q\left(\frac{\frac{d}{R_1}s_1}{\sigma_n}\right) ds_1\right). \tag{8}$$

Jumping to the upper level occurs when $n > d - \frac{d}{R_1}s_1$. In this case, the estimation errors are $\hat{s}_1 - s_1 = e_{1r}$ and $\hat{s}_2 - s_2 = \lambda_y + e_{2r}$ where $|e_{1r}| = |n - d|$ and $|e_{2r}| = \Delta$. Therefore, one can express $\mathrm{MSE}_{\mathrm{rc}}$ as

$$\mathrm{MSE}_{\mathrm{rc}} = \left(\mathbb{E}\left\{|e_{1r}|^2\right\} + \mathbb{E}\left\{|e_{2r}|^2\right\} + \mathbb{E}\left\{|\lambda_y|^2\right\}\right) p_{rc}. \tag{9}$$

Following the assumption of AWGN, the probability of right stage crossing p_{rc} is given by

$$p_{rc} = \mathbb{P}\left\{n > d - \frac{d}{R_1}s_1\right\} = \int_0^{R_1} p_1(s_1)\ Q\left(\frac{d - \frac{d}{R_1}s_1}{\sigma_n}\right) ds_1. \tag{10}$$

Similarly, jumping to the lower level occurs when $n < -\frac{d}{R_1}s_1$. The estimation errors in such case are $\hat{s}_1 - s_1 = e_{1l}$ and $\hat{s}_2 - s_2 = \lambda_y + e_{2l}$ where $|e_{1l}| = |n - d|$ and $|e_{2l}| = \Delta$. Therefore, $\mathrm{MSE}_{\mathrm{lc}}$ is expressed in a similar way to (9) with the probability of left stage crossing p_{lc} given by

$$p_{lc} = \mathbb{P}\left\{n < -\frac{d}{R_1}s_1\right\} = \int_0^{R_1} p_1(s_1)\ Q\left(\frac{\frac{d}{R_1}s_1}{\sigma_n}\right) ds_1. \tag{11}$$

It follows that the overall probability of stage crossing is $p_s = p_{rc} + p_{lc}$.

From the above analysis, it can be noticed that p_m, p_{rc} and p_{lc} are highly dependent on the PDF of s_1. Moreover, one may intuitively deduce that stage crossing is likely to happen when the mapped point of s_1 lies on the boundaries. The probability of occurrence of such event is minimized when the PDF of s_1 is centralized around its mean and has a decaying tail (e.g., Gaussian PDF). Considering these types of bell-shaped PDFs, the worst case for stage crossing occurs when s_1 follows a uniform distribution. In that case, the probability of mapping s_1 on the boundary is exactly equal to the probability of mapping s_1 on any other point on the line. Therefore, an upper bound on the probability of stage crossing for bell-shaped PDFs can be obtained by assuming $s_1 \sim \mathrm{U}[0, R_1]$.

Lemma 1: The probability of stage crossing for bell-shaped PDFs is upper bounded by

$$p_s^{\mathrm{up}} = \frac{2\sigma_n}{d\sqrt{2\pi}}\left(1 - e^{-\frac{1}{2}\left(\frac{d}{\sigma_n}\right)^2} + \sqrt{2\pi}\left(\frac{d}{\sigma_n}\right) Q\left(\frac{d}{\sigma_n}\right)\right). \tag{12}$$

Proof. See Appendix A.

The corresponding upper bound on the MSE part due to the recovery of s_1 is given by

$$\mathrm{MSE}_1^{\mathrm{up}} = \frac{R_1^2 L^2}{\gamma^2}\sigma_n^2\, p_m + \underbrace{d^2 p_s^{\mathrm{up}}}_{\mathrm{MSE}_{sc_1}^{\mathrm{up}}}. \tag{13}$$

Similary, the upper bound on the MSE part due to the recovery of s_2 can be written as

$$\mathrm{MSE}_2^{\mathrm{up}} = \frac{1}{12}\frac{R_2^2}{(L-1)^2}\, p_m + \underbrace{\Delta^2 p_s^{\mathrm{up}}}_{\mathrm{MSE}_{sc_2}^{\mathrm{up}}}. \tag{14}$$

In our considered setup, due to the presence of a strong LOS, it is reasonable to assume a high SNR with $d^2 \gg \sigma_n^2$. In such scenario, the probability of stage crossing p_s is negligible and $p_m \approx 1$ as will be shown in Sec. VI. Consequently, the overall MSE is given by

$$\mathrm{MSE} \approx \mathrm{MSE}_{\mathrm{mid}} = \frac{R_1^2 L^2}{\gamma^2}\sigma_n^2 + \frac{1}{12}\frac{R_2^2}{(L-1)^2}. \tag{15}$$

The closed form MSE expression in (15) is verified through numerical simulations as will be discussed in Sec. VI. One can notice that performance of the mapping depends on both L and γ. Therefore, for a given value of γ, there exists an optimal value of L that optimizes the performance under the constraint given by $dL = \gamma$.

Remark 1: Since low-power sensing schemes are considered in this work, the closed form MSE expression obtained from ML decoding in (15) is used at the sensing node to optimize the mapping parameters. Low-complexity computations at the sensing nodes are essential to provide optimized yet simple compression. It is worth mentioning that, in [31, Sec. VII], it has been shown that the performance gap of applying minimum mean squared error (MMSE) decoding to recover data from compression mappings optimized for ML decoding and those optimized for MMSE decoding is negligible. Our conducted simulations verified these findings for our proposed mapping. However, since MMSE optimization can only be performed numerically with no closed form analytical expressions, the details of MMSE optimization and decoding are out of scope and are omitted from this work.

Remark 2: It should be pointed out that the obtained MSE expression in (15) from the triangular mapping for the high SNR case is exactly the same as that of the rectangular mapping which can be found in [15, Eq. 5]. It can then be deduced that the triangular mapping has the same performance as the rectangular mapping despite having a much lower complexity circuit implementation.

B. Optimization of the mapping

In this subsection, we discuss optimizing the parameters of the triangular mapping with the goal of minimizing the MSE (distortion) at the receiver. Two different ways of formulating the optimization problem are discussed. The first formulation deals with optimizing parameters of the mapping subject to a power constraint with the goal of minimizing the MSE. The other formulation discusses finding the parameters of the mapping that minimizes the used power subject to an MSE threshold.

1) Optimizing the mapping to minimize the MSE at the receiver: Generally, it is more common to optimize compression mappings given an average power constraint instead of a voltage constraint (e.g., constraint on γ). For that purpose, the calculation of the quantity $\mathbb{E}\left\{f^2(\mathbf{s})\right\}$ is required. We assume, for the sake of tractability, that the source signals follow a uniform distribution. Therefore, $s_2 \sim \mathrm{U}\left[0, R_2\right]$. By definition of $k = \mathrm{round}(\frac{s_2}{\Delta})$, it can be easily shown that k is also uniformly distributed in $[0, L-1]$. Consequently, one can write $\mathbb{E}\left\{k\right\} = \frac{L-1}{2}$ and $\mathbb{E}\left\{k^2\right\} = \frac{(2L-1)(L-1)}{6}$. For the proposed triangular mapping encoding function in (1), $\mathbb{E}\left\{f^2(\mathbf{s})\right\}$ is then expressed as

$$\begin{aligned}\mathbb{E}\left\{f^2(\mathbf{s})\right\} &= d^2\left[\mathbb{E}\left\{k^2\right\} + \frac{2\mathbb{E}\left\{k\right\}\mathbb{E}\left\{s_1\right\}}{R_1} + \frac{\mathbb{E}\left\{s_1^2\right\}}{R_1^2}\right] \\ &= \frac{d^2L^2}{3}.\end{aligned} \tag{16}$$

In the following sections of the paper, for simplicity, the constant fraction $1/3$ is omitted and $\gamma^2 = P_{\max}$ is assumed as the power constraint at the encoder. It should be pointed out that if the distribution of the source signals is different from uniform, this constraint can be viewed as the maximum encoding power instead of the average encoding power. The optimal MSE for a given $P_{\max}$ using triangular mapping is obtained from solving the following optimization problem

$$\begin{aligned}\min_{L} \quad & (15) \\ \text{subject to} \quad & (dL)^2 \leq P_{\max}\end{aligned}. \tag{17}$$

The above problem is jointly convex in $(L\,, d)$ and can easily be solved using convex optimization tools such as CVX [32].

2) Optimizing the mapping given an MSE threshold: An alternative optimization problem can be formulated to obtain the parameters of the mapping (i.e., L and d) that minimizes the power subject to an MSE threshold ϵ as follows

$$\begin{aligned}\min_{L,\,d} \quad & d^2L^2 \\ \text{subject to} \quad & \mathrm{MSE} \leq \epsilon\end{aligned}. \tag{18}$$

The above alternative optimization problem is also jointly convex in $(L,\, d)$ and can be solved using CVX. At this point, we would like to stress that, in the considered wirelessly powered sensors scenario, the formulation described in (17) is more applicable. However, the alternative formulation is presented here for the sake of completeness and in order to study the effect of changing L and d on the MSE performance.

IV. Improving the triangular mapping to minimize Distortion

In this section, we consider different techniques to improve the distortion performance of the proposed mapping. We first study mapping adaptation to the PDFs of the source signals assuming that they are uncorrelated. Then, different types of correlation between the source signals are studied and exploited to improve the distortion of the mapping. Through this section, we refer to the MSE at the receiver as the distortion and denote it by D. Although the studies conducted in this section are in the context of the proposed triangular mapping, they are actually applicable to other types of AJSCC mappings.

A. PDF-adaptive Quantizer for improving the distortion error

In the previous section, the triangular mapping was assumed to have uniform spacing between levels (i.e., Δ). In fact, this assumption achieves the best performance if s_2 follows a uniform distribution. However, if s_2 follows a different probability distribution other than uniform, the use of non-uniform quantization can possibly improve the distortion error performance. One can intuitively think of allocating different number of levels to different regions of the PDF depending on the probability distribution. That is to say, more levels are allocated to regions of higher probability. The distortion part due to the quantization error in this case is given by

$$D_{q_{s_2}} = \sum_{i=1}^{N_R} \mathbb{P}_{s_2 \in \text{ Region i}} D_{q_i}, \tag{19}$$

where D_{q_i} is the quantization error in region i and N_R is the number of regions.

The above discussion is well-known within the frame work of quantization. Non-uniform quantizers such as the Lloyd-max iterative algorithm are typically used in that context of finding the optimal quantizer for a given PDF [28], [33], [34]. However, the Lloyd-max algorithm finds the optimal quantizer (it outputs the optimal decision thresholds) for a given number of levels. In our setup, the goal is to find the optimal number of levels which minimizes the distortion. Therefore, we use an adaptive quantizer inspired by the Lloyd-max algorithm. In such adaptive quantizer, the decision threshold is fixed at the center between each two consecutive levels. The number of quantization levels in different regions varies differently according to the PDF.

An example to illustrate the adaptive quantizer is shown in Fig. 5. Here, we assume s_2 follows a Gaussian distribution. In this case, the further from the mean, the lower the probability of s_2. The PDF of s_2 decays as we move from the 1σ region to the 3σ until it approaches zero beyond the 3σ region. Therefore, it is reasonable to put more levels in the 1σ region and decrease the number of quantization levels in the regions of lower probability of occurrence of s_2. In the considered example illustrated in Fig. 5, the total distortion due to quantization consists of: the granular distortion which can be controlled with the number of quantization levels, and the overload distortion due to the infinite boundaries of the Gaussian distribution. Due to the decaying tail probability after the 3σ region and the uncontrollable nature of the overload distortion, we set our focus on improving the average granular distortion.

To improve the average distortion in the 3σ region, we divide it into three[3] sub-regions (defined at 1σ, 2σ and 3σ). Each region has a different number of quantization levels. Inside each region, the quantization levels are equally separated by Δ_i with $i \in \{1, 2, 3\}$ as shown in Fig. 5. In this case, the average distortion due to quantization denoted by D_{avg} is expressed as

$$\begin{aligned} D_{\text{avg}} =& \mathbb{P}_{s_2 \in \text{ Region 1}} D_{\Delta_1} + \mathbb{P}_{s_2 \in \text{ Region 2}} D_{\Delta_2} \\ &+ \mathbb{P}_{s_2 \in \text{ Region 3}} D_{\Delta_3}, \end{aligned} \tag{20}$$

[3]The idea is applicable to divisions into more than three sub-regions.

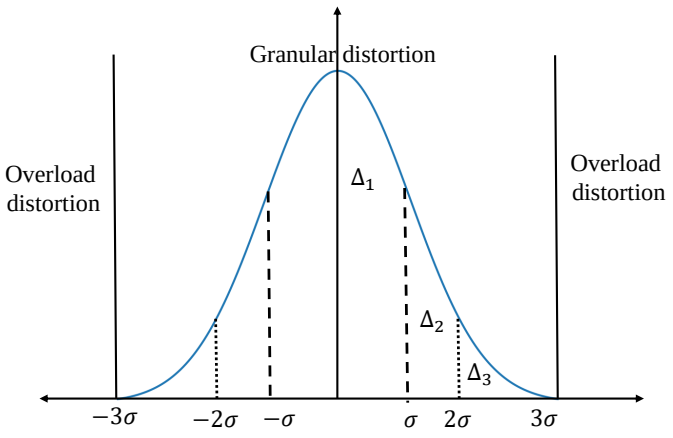

Fig. 5. An example of non-uniform quantization in the Gaussian source case.

where $\mathbb{P}_{s_2 \in \text{ Region } i}$ represents the probability that the source signal lies in region i and is obtained from the probability distribution function of s_2. It has been shown in [28, Ch. 5.4] that, for high resolution uniform quantization, the quantization error is independent of the input distribution and is equal to $\frac{\Delta^2}{12}$. Therefore, the total average distortion (i.e., MSE_{tot}) can be written as

$$\begin{aligned} D_{\text{tot}} =& \frac{1}{12} \left(\mathbb{P}_{s_2 \in \text{ Region 1}} \Delta_1^2 + \mathbb{P}_{s_2 \in \text{ Region 2}} \Delta_2^2 \right. \\ &\left. + \mathbb{P}_{s_2 \in \text{ Region 3}} \Delta_3^2 \right) + \frac{R_1^2}{d^2} \sigma_n^2. \end{aligned} \tag{21}$$

Here, the total number of levels is equal to $L_1 + L_2 + L_3$. An optimization problem can be formulated to minimize (21) subject to the constraint on the maximum power that is given by $d^2(L_1 + L_2 + L_3)^2 \leq P$. The optimization problem in this case is still convex in $L_i \, \forall \, i$ and d and can be solved using CVX.

The above described adaptive quantizer can be implemented by adding an analog comparator connected to s_2 in Fig. 4 in order to determine the region. The output of comparator then selects one of three branches each containing a voltage divider and an analog multiplier with Δ_i and d, respectively. The output of the selected branch is added with the bottom branch coming from s_1 as before.

B. Exploiting Different types of correlation between sensor signals in refining the compression mapping

1) Temporal correlation: In this subsection, we assume that a temporal correlation exists between the source signals. Such correlation can exist if the sensor readings are slowly varying with respect to the timestamps over which they are recorded. In this paper, we model the temporal correlation by a first-order Markov process [35] as follows

$$s_{i,t} = \alpha s_{i,t-1} + \sqrt{1 - \alpha^2} w_{t-1}, \;\; i = 1, 2 \quad \forall t = 1, 2, \ldots, \tag{22}$$

where $|\alpha| < 1$ represents the correlation coefficient and w_t is an independent and identically distributed process such that $w_t \sim (0, \; \sigma_w^2)$ whereas $s_{i,0}$ is the initial reading of sensor i and is independent of w_t. It should be pointed out that the

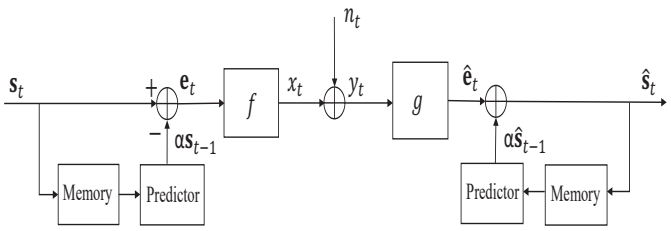

Fig. 6. Using differential coding with triangular mapping.

problem of AJSCC for a temporally correlated source has been discussed previously in the literature, for example in [36] (see also the references therein). However, different from the existing work in the literature, we do not discuss finding the optimal design of AJSCC to exploit the temporal correlation between the source signals. Instead, we study how to adapt our proposed low-complexity triangular mapping to these types of correlation to improve its distortion error performance.

We propose the use of differential coding [28, Ch. 7] combined with triangular mapping in order to exploit the temporal correlation. The resulting improvement in the distortion at the receiver is investigated. The proposed scheme is illustrated in Fig. 6 and described as follows. The encoder is assumed to have memory of the previous sensors' readings and is equipped with a linear predictor. Instead of applying the triangular mapping encoding function (i.e., $f(.)$) on $\mathbf{s}_t$, the encoding function is applied to $\mathbf{e}_t$. We define $\mathbf{e}_t = (e_{1,t}\ e_{2,t})^T$ as the innovation at time t. At time t, the encoder calculates the quantity[4] $\alpha\mathbf{s}_{t-1}$ based on its memory of $\mathbf{s}_{t-1}$ using the linear predictor. Then, it calculates the innovation as follows

$$e_{i,t} = s_{i,t} - \alpha s_{i,t-1},\ i = 1, 2. \tag{23}$$

The calculated values of $e_{1,t}$ and $e_{2,t}$ are mapped into the triangular mapping generating x_t which is then transmitted through the channel. The mean of $e_{i,t}$ is calculated using (22) and (23) as follows

$$\mathbb{E}\{e_{i,t}\} = \mathbb{E}\{w_{t-1}\} = 0,\ \forall t = 1, 2, \ldots. \tag{24}$$

Similarly, the variance of $e_{i,t}$ is equal to $\left(1-\alpha^2\right)\sigma_w^2$. Typically, this indicates that the input to the encoding function now has a smaller mean and variance than the original source signals. Therefore, at time t, the power available at the encoder which is reflected by the number of levels and the length of each level in the triangular mapping will be focused on smaller range of values, and thus, the mapping resolution increases.

At the receiver, similar to the encoder, the decoder is assumed to have memory of the previous estimated readings and equipped with a linear predictor. The decoder first estimates the AJSCC coded signal $\hat{\mathbf{e}}_t$. If an additive Gaussian noise is assumed here, the triangular mapping is chosen to cover the range $[-2\sigma_w\sqrt{(1-\alpha^2)}, 2\sigma_w\sqrt{(1-\alpha^2)}]$ for each of e_1 and e_2. Therefore, we can express

$$\mathbb{E}\left\{\left|\hat{\mathbf{e}}_t - \mathbf{e}_t\right|^2\right\} = \left(1-\alpha^2\right)\left(\frac{\left(4\sigma_w\right)^2\sigma_n^2}{d^2} + \frac{\left(4\sigma_w\right)^2}{12\left(L-1\right)^2}\right). \tag{25}$$

After estimating the value of $\hat{\mathbf{e}}_t$, the decoder utilizes the temporal correlation to calculate $\hat{\mathbf{s}}_t$ using

$$\hat{\mathbf{s}}_t = \hat{\mathbf{e}}_t + \alpha\hat{\mathbf{s}}_{t-1}. \tag{26}$$

One can express $\hat{\mathbf{e}}_t$ as

$$\hat{\mathbf{e}}_t = \mathbf{s}_t - \alpha\mathbf{s}_{t-1} + \mathbf{q}, \tag{27}$$

with $\mathbf{q}$ being the reconstruction error vector[5]. From (26) and (27), the end-to-end distortion can be expressed as

$$\mathbb{E}\left\{\left|\hat{\mathbf{s}}_t - \mathbf{s}_t\right|^2\right\} = \alpha^2\mathbb{E}\left\{\left|\hat{\mathbf{s}}_{t-1} - \mathbf{s}_{t-1}\right|^2\right\} + \left(1-\alpha^2\right)\left[\frac{\left(4\sigma_w\right)^2\sigma_n^2}{d^2} + \frac{\left(4\sigma_w\right)^2}{12\left(L-1\right)^2}\right]. \tag{28}$$

The above analysis shows how triangular mapping can be combined with differential coding in order to exploit the temporal correlation between the source signals in improving the distortion. A convex optimization problem can be formulated to minimize (28) as a function of d and L subject to a power constraint similar to that discussed in the previous sections. A further improvement can be achieved when the method in (20) is applied to encode $\mathbf{e}_t$. It is worth mentioning that the differential coding described in this subsection is beneficial in the low SNR scenario because it minimizes the error due to stage crossing.

2) Correlation between source signals: So far, in the previous subsection, we considered that the source signals are correlated in time. In this subsection, we consider that the sensor readings (s_1 and s_2) are correlated and discuss the effect of this correlation on our proposed triangular mapping. In general, for linear correlation models, one can find a linear decorrelating transformation which is basically a rotation. AJSCC for correlated sources has been discussed in [22], [35], [37]. In [35], PCCOVQ algorithm was used to obtain JSCC mappings in the case of correlated source signals. It has been found that the optimal mapping is a rotated version of the mapping in the uncorrelated case. This fact has also been pointed out in [22], [37]. In order to model the correlation between the source signals, we assume that $\mathbb{E}\{s_1 s_2\} = \rho\sigma_{s_1}\sigma_{s_2}$. To efficiently maximize the source space (the blue dots in Fig. 7) covered by the triangular mapping, the mapping is rotated with an angle β as shown in Fig. 7. The rotation is performed to encode the decorrelated parts of the source signals. The rotation of axis obtained by applying the transformation

$$\begin{pmatrix} s_1' \\ s_2' \end{pmatrix} = \begin{pmatrix} \cos\beta & \sin\beta \\ -\sin\beta & \cos\beta \end{pmatrix}\begin{pmatrix} s_1 - \mu_1 \\ s_2 - \mu_2 \end{pmatrix} + \begin{pmatrix} \mu_1 \\ \mu_2 \end{pmatrix}\cos\beta, \tag{29}$$

[4]For negative correlation (i.e., $\alpha < 0$), the encoder calculates $-\alpha\mathbf{s}_{t-1}$ instead.

[5]Note that $\mathbb{E}\left\{|\mathbf{q}|^2\right\} = \mathbb{E}\left\{\left|\hat{\mathbf{e}}_t - \mathbf{e}_t\right|^2\right\}$. In addition, it is worth mentioning that $\mathbf{q}$ is orthogonal on both $\mathbf{s}_t$ and $\hat{\mathbf{s}}_t$.

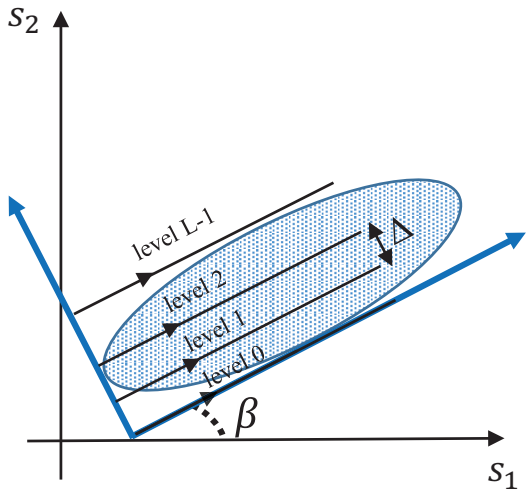

Fig. 7. Rotation of the mapping to decorrelate the sources.

with

$$\beta = \tan^{-1}\rho, \tag{30}$$

$\mu_1 = \frac{R_1}{2}$ and $\mu_2 = \frac{R_2}{2}$ in the case of uniformly distributed s_1 and s_2. After applying the rotation of axis in (29), the decorrelated source points (s'_1 and s'_2) are encoded using the triangular mapping in the same way as described in Sec. II-B. The resulting MSE expression after rotation of axis becomes

$$\text{MSE}_{Rot} = \frac{(R_1\cos\beta)^2 L^2}{\gamma^2}\sigma_n^2 + \frac{1}{12}\frac{(R_2\cos\beta)^2}{(L-1)^2}. \tag{31}$$

It can noticed that the MSE resulting from the rotation of mapping is lower than the case of no rotation due to the factor $\cos\beta$. We would like to point out that, for the case of correlated source signals that are also correlated in time, the mapping is first rotated to decorrelate the sources, and then the temporal correlation is exploited, for example by applying the differential coding to $s'_{1,t}$ and $s'_{2,t}$.

In order to avoid the complexity in implementing the sinusoidal functions using analog circuits, one can implement a number of predefined rotations as scaling factors to s_1 and s_2. These predefined rotations should be switchable according to the correlation between s_1 and s_2.

V. AJSCC for Sensors with Energy Scheduling Capabilities

In a wirelessly-powered sensor scenario such as the one considered in this paper, each sensing node utilizes its harvested power to optimize the parameters of the mapping with the goal of minimizing the distortion error at the receiver. Typically, each sensor node is equipped with a battery to operate its circuitry and to carry out the measurement and the encoding processes. In this section, we assume that each sensor node is capable of scheduling and managing its harvested power over time. Energy management policies have been studied before in the context of maximizing the throughput of wirelessly-powered communication nodes such as in [38] and references therein. However, to the best of the authors' knowledge, this is the first work within the framework of low-power sensors

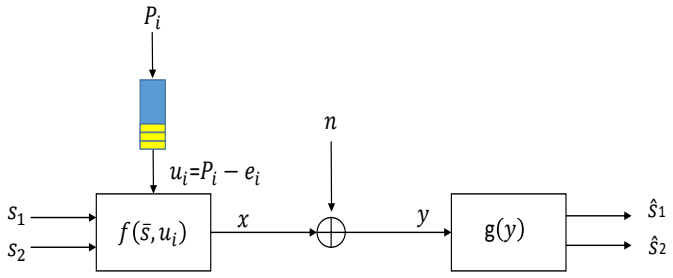

Fig. 8. Block diagram of AJSCC with energy scheduling.

that considers the problem of energy scheduling in optimizing low-complexity AJSCC dimension reduction mappings with the goal of minimizing the distortion at the receiver.

As described in Fig. 8, at each time instant i, a power P_i is assumed to arrive at the sensing node from the HAP through energy harvesting. Furthermore, we assume a linear energy harvesting model at the sensor node[6] meaning that harvested power at the sensor node is a fixed fraction of the incoming RF power at each time instant (i.e., $P_i = \eta P_{\text{RF}}$), with η being the energy harvester efficiency. At each time instant, we assume that a power $e_i \geq \tau$ is reserved to energize the sensor circuitry with τ being the minimum power required to operate the sensor circuit. Consequently, the available power for the encoder is given by $u_i = P_i - e_i$ (i.e., $d_i^2 L_i^2 = P_i - e_i$). In this section, we assume that the sources are uncorrelated. This is due to the fact that uncorrelated sources represent the worst case MSE performance. Therefore, the MSE at time i can be expressed as

$$\text{MSE}_i = \frac{L_i^2 R_1^2}{(P_i - e_i)}\sigma_n^2 + \frac{1}{12}\frac{R_2^2}{(L_i-1)^2}. \tag{32}$$

In the case of correlation between the source signals, the expressions in (25) and (31) can replace the one in (32). The mapping optimization problem at each instant i is written as

$$\begin{aligned} \min_{L_i,\, u_i} \quad & \text{MSE}_i \\ \text{subject to} \quad & u_i \leq P_i - \tau \;\forall\, i = 1, ..., N \end{aligned} \tag{33}$$

In order to obtain a feasible solution, the harvested power P_i is assumed to be always greater than or equal τ to avoid the event of energy shortage[7] at the sensor node. The above problem formulation assumes that power arriving at the i^{th} time instant can only be used instantaneously (i.e., no power can be saved in the battery for later use). However, as discussed above, the encoder at the sensing node may exploit the presence of the battery to schedule energy for later use. This is beneficial for the total distortion (sum MSE) over the whole time horizon in the case of low power arrival instants. We further assume that the sensor node knows a priori the power arrivals for the time frame N. This is done by the HAP at the beginning of each

[6]A linear energy harvesting model is a reasonable assumption if the input power to the harvester is in the range of hundreds of μwatts [39] or if a single-tone signal is used for WPT.

[7]One might as well assume that the sensor node relies on other energy harvesting sources to operate its circuit.

time frame in the training and channel estimation phase. In that phase, the HAP is assumed to perform channel estimation and decision on how to allocate its available power for the different sensor nodes during the time frame N following its optimized trajectory. The HAP stores the power transmission codebook and sends it to the sensor node in this training phase. The optimization problem at the sensor node with energy scheduling capability is given by

$$\begin{array}{ll} \min\limits_{L_i,\,u_i} & \sum_{i=1}^{N} \frac{L_i^2 R_1^2}{u_i}\sigma_n^2 + \frac{1}{12}\frac{R_2^2}{(L_i-1)^2} \\ \text{subj} & \sum_{j=1}^{m} u_j \leq \sum_{j=1}^{m} (P_j - \tau) \;\; \forall\, m = 1, ..., N \end{array} \tag{34}$$

In the above formulation, we assume that the battery size B is sufficiently greater than the maximum possible saved power ($B \geq \arg\max_i P_i - \tau$). This is equivalent to assumption of unlimited-sized battery in [38].

Since u_i and L_i are both greater than zero, the objective function is jointly convex in $(u_i,\, L_i)$. In addition, the constraint set is convex as it is composed of linear constraints. Hence, the above optimization problem is a convex optimization problem with unique minimizers $\mathbf{u}^*$ and $\mathbf{L}^*$, where $\mathbf{u}^* = [u_1, u_2, ..., u_N]^T$ and $\mathbf{L}^* = [L_1, L_2, ..., L_N]^T$. We define the Lagrangian function for the above optimization problem as follows

$$\begin{aligned} J(L_i,\, u_i, \lambda_i) =& \sum_{i=1}^{N} \left(\frac{L_i^2 R_1^2}{u_i}\sigma_n^2 + \frac{1}{12}\frac{R_2^2}{(L_i-1)^2} \right) - \\ & \sum_{l=1}^{N} \lambda_l \left(\sum_{j=1}^{l} u_j - \sum_{j=1}^{l} (P_j - \tau) \right). \end{aligned} \tag{35}$$

The additional complementary slackness condition is

$$\lambda_l \left(\sum_{j=1}^{l} u_j - \sum_{j=1}^{l} (P_j - \tau) \right) = 0, \quad l = 1, ..., N. \tag{36}$$

The necessary and sufficient KKT conditions are given by

$$\frac{\partial J}{\partial L_i} = \sum_{i=1}^{N} \left(\frac{2 L_i R_1^2}{u_i}\sigma_n^2 - \frac{1}{6}\frac{R_2^2}{(L_i-1)^3} \right) = 0, \tag{37}$$

$$\frac{\partial J}{\partial u_i} = \sum_{i=1}^{N} \left(-\frac{L_i^2 R_1^2}{u_i^2}\sigma_n^2 - \lambda_i \right) = 0, \tag{38}$$

$$\sum_{j=1}^{l} (u_j - (P_j - \tau)) \leq 0 \quad l = 1, ..., N, \tag{39}$$

$$\lambda_l \geq 0 \quad l = 1, ..., N. \tag{40}$$

From (37), one can write the relation between L_i and u_i as

$$L_i (L_i - 1)^3 = \frac{1}{12}\frac{R_2}{R_1^2 \sigma_n^2} u_i. \tag{41}$$

It should be noted that any power vector with $\sum_{j=1}^{N} u_j < \sum_{j=1}^{N} (P_j - \tau)$ is suboptimal because the objective function is monotonically decreasing in u_i.

Proposition 1: For a fixed L_i, the objective function in (34) is Schur convex in u_i. Therefore, the optimal power allocation vector $\mathbf{u}^* = [u_1, u_2, ..., u_N]^T$ that minimizes the objective function is the most majorized feasible power vector [40, Sec. V], [41].

Since $\frac{1}{x}$ is convex for $x \geq 0$, the objective function in (33) is convex in u_i. Therefore, it is also Schur convex [41]. The optimal power vector $\mathbf{u}^*$ is the most majorized feasible power vector, i.e., $\mathbf{u}^* \preceq \mathbf{u}$ for all feasible $\mathbf{u}$. As discussed in [40, Sec. 5], the uniform power vector is majorized by every other feasible vector. This means that, if the vector of constant powers $u_i = \frac{\sum_{i=1}^{N}(P_i - \tau)}{N}$ is feasible, then it is majorized by any other feasible vector and optimally solves (34), i.e., the optimal u_i tends to be as constant as possible over time. However, due to the causality of power arrivals, the constant power vector may not be in the feasible set (i.e., power arriving at later time instants cannot be used before their arrivals).

The energy scheduling problem presented in (33) can easily be solved using a convex optimization solver such as CVX. However, since a low-power sensor node is considered in our scenario with limited computational resources, it is favorable to save time and complexity resulting from the use of CVX. For this reason, we propose Algorithm 1 to find the optimal u_i. Then, the relation in (41) is applied to obtain the corresponding L_i. The proposed algorithm is compared to CVX in terms of the average computational time needed to execute each in Sec. VI (see Table I) indicating a much faster performance for Algorithm 1.

We would like to point out that tuning the mapping parameters (d and Δ) over time can be done by connecting their corresponding voltages in Fig. 4 to a tunable voltage divider circuit which can easily be implemented using variable resistors.

Algorithm 1 Optimum power scheduling algorithm.

Initialize: $i = 1$
While $i \leq N$ **do**:
  set $j = i$
  While $j \leq N$
    if $P_i \geq P_j$, set $j = j + 1$
    else break
  set $u_m = \frac{\sum_{k=i}^{j-1}(P_k - \tau)}{j - i}$ $\forall m = 1, .., j-1$
  set $i = j$
Compute L_i from u_i using (41) $\forall i = 1, .., N$
Return $\mathbf{u}$ and $\mathbf{L}$
End

VI. Simulation Results

In this section, we evaluate the performance of our proposed triangular mapping and verify the presented analytical expressions in the paper. Moreover, we show simulation results for the mapping improvement techniques discussed in Sec. IV as well as the energy scheduling problem presented in Sec. V. Throughout this section, we assume that the noise power σ_n^2 is 1×10^{-9} (i.e., -60 dBm) and $R_1 = R_2 = 1$ unless otherwise is mentioned.

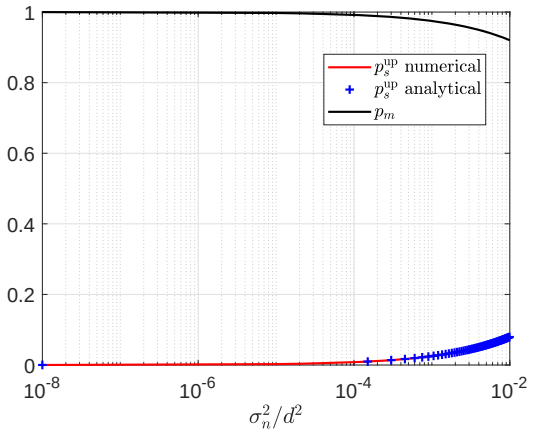

Fig. 9. Validation of the upper bound on the probability of stage crossing p_s^{up} vs. $\frac{\sigma_n^2}{d^2}$.

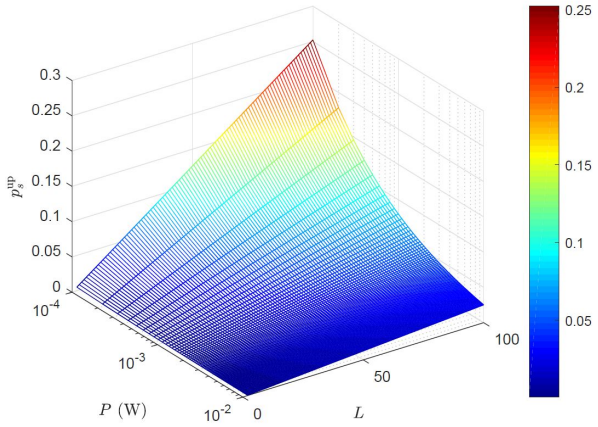

Fig. 10. Study of the upper bound on the probability of stage crossing p_s^{up} vs. the number of levels and available power.

A. Verifying the MSE performance of the proposed triangular mapping

We start by showing that the probability of stage crossing can be neglected for if $d^2 \gg \sigma_n^2$ as discussed in Sec. III-A. In Fig. 9, we show a study of the upper bound on the probability of stage crossing (p_s^{up}) in (12) vs. σ_n^2/d^2. It can be observed that, as long as $\sigma_n^2 \ll d^2$, the probability of stage crossing is negligible. In addition, the analytical expression for p_s^{up} given in (12) is validated through comparison with the numerical evaluation of the expressions in (10) and (11) as shown in Fig. 9.

In Fig. 10, a study of p_s^{up} vs. both the available power (P) and the number of levels (L) is conducted. It can be noticed that as P increases, p_s^{up} becomes negligible. On the other hand, for a fixed power, p_s^{up} increases if the number of levels becomes large. This is because as L increases under a fixed power constraint, d becomes smaller, and thus, p_s^{up} increases.

Finally, we verify the analytical MSE expression for the high SNR case given in (15). For that purpose, we assume s_1 and s_2 are uniformly distributed with $R_1 = R_2 = 1$ and $\gamma = 50$. A study of the different components of the MSE vs. the number of levels (L) is conducted in Fig. 11. For each value of L, ten thousand realizations of s_1 and s_2 were generated and the average numerical MSE for recovering s_1 and s_2 was computed. A comparison of the numerical simulation of the MSE and that obtained using the analytical expression is presented in Fig. 11. An excellent agreement between the numerical and the analytical MSE computation can be noticed. Moreover, one can notice that the error in recovering s_2 decreases as L increases due to the minimization of the quantization error. However, the error in recovering s_1 increases as L increases because the value of d becomes smaller.

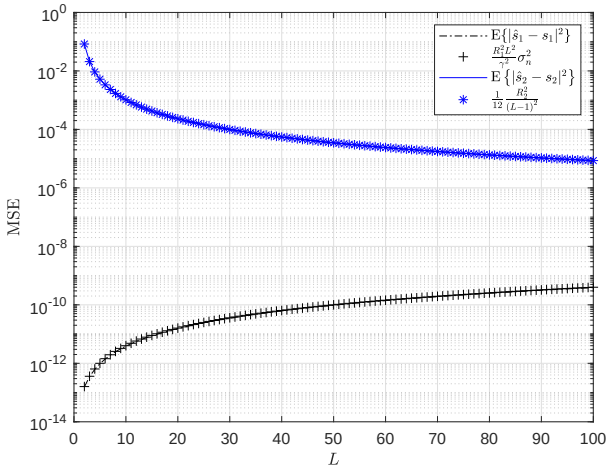

Fig. 11. Comparison of the analytical MSE expressions vs. numerical simulations.

B. Results for optimizing the mapping parameters for minimizing the MSE

In this subsection, we compare the optimal MSE performance for a given power P for different types of mapping; the proposed triangular mapping, linear coding [42], and Archimedean spiral [18], [25], [43]. The importance of conducting such comparison is due to the fact that linear policies serve as a benchmark and are the easiest to be implemented. The optimal solution for the triangular mapping is obtained from solving (17) while the optimal linear coding solution is obtained from [42, Sec. V] and that of the Archimedean spiral is obtained from [18].

We assume that $s_1 \sim \mathcal{N}(0,\ 1)$ and $s_2 \sim \mathcal{N}(0,\ 1)$. The triangular mapping is chosen to cover the region $[-3\sigma_s, 3\sigma_s]$ (i.e., $[-3, 3]$). The optimized MSE computed as $\frac{1}{2}\mathbb{E}\left\{|\hat{s}_1 - s_1|^2\right\} + \frac{1}{2}\mathbb{E}\left\{|\hat{s}_2 - s_2|^2\right\}$ vs. $P_{\max}$ is plotted in Fig. 12 for linear, triangular and spiral mapping. It can be observed that triangular mapping highly outperforms the optimal linear mapping. This is because in 2:1 compression using linear mapping, the optimal decoder choose to recover one source signal correctly all the time while the other signal is recovered randomly or set to zero [22], [42]. Furthermore, the proposed triangular mapping maintains a good performance compared to the spiral mapping taking into account the much

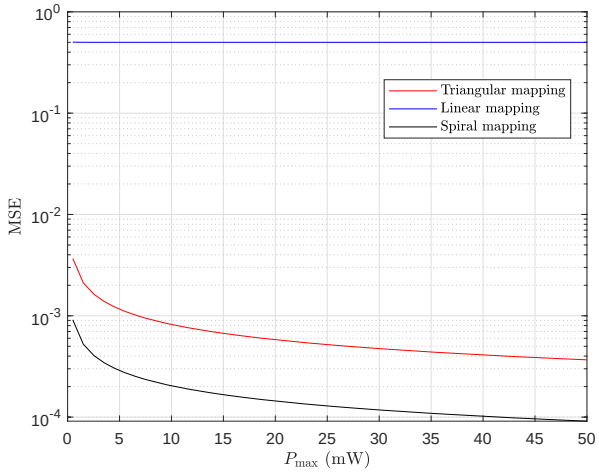

Fig. 12. Comparison of the optimal MSE performance vs. $P_{\max}$ for the proposed triangular mapping, linear coding and spiral mapping.

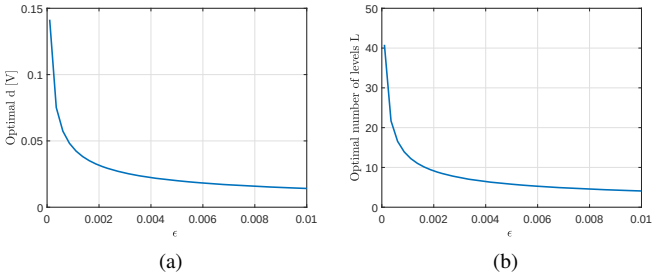

Fig. 13. (a) Study of the optimal voltage per level d vs. the MSE threshold ϵ. (b) Study of the optimal number of levels L vs. the MSE threshold ϵ.

lower implementation complexity. We would like to emphasize that the optimal performance of the proposed triangular mapping in a high SNR scenario is exactly the same as that of the rectangular mapping in [14] as previously pointed out in *Remark 2*.

In Fig. 13(a) and Fig. 13(b), the MSE threshold (ϵ) is varied and the results of the optimization problem in (18) given by d and L are plotted for uniformly distributed s_1 and s_2 with $P = 1$ mW and $\sigma_n^2 = 1\times10^{-6}$. One can notice that as the threshold decreases, the values of L and d increase. Increasing L and d results in increasing the encoding power ($P = \mathbb{E}\left\{f^2(\mathbf{s})\right\}$).

C. Applying the proposed triangular mapping to real IoT data sets

Here, we apply our proposed triangular mapping as well as the linear and the spiral mapping to the data in [44]. The considered data is obtained from sensors deployed in an agriculture field to monitor volumetric water (VW) content and the temperature of the soil. The measurement setup is described in [45]. We applied our mapping to the measurement data obtained during the month of April 2016 with sensors positioned at 0.6 mm depth at location $CAF007$. VW content measurements are used as s_1 while the temperature measurements are used as s_2. The calculated mean of s_1 and s_2 is

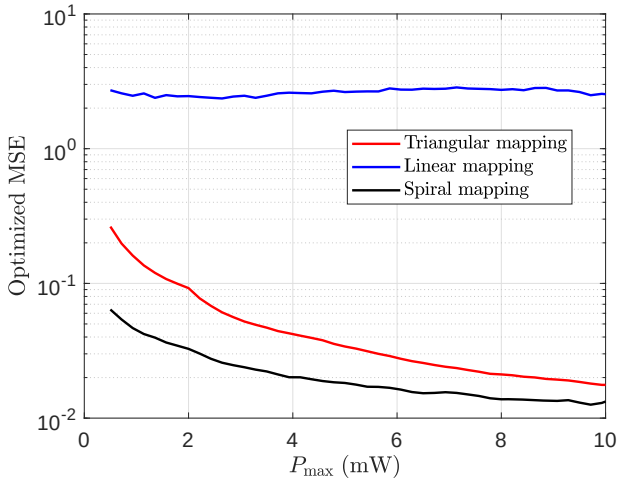

Fig. 14. Optimized MSE for data from agriculture sensors in [44].

0.2814 and 11.1468, respectively. The variance is 3.274×10^{-5} and 2.7359 for s_1 and s_2, respectively. The distribution of each sensor's data is approximated to a Gaussian distribution. For different available powers assumed at the sensing node, the optimal choices of L and d are obtained by solving the optimization problem in (17). A plot of the optimized MSE for the above described data vs. the available power is shown in Fig. 14. It can be noticed that the MSE value decreases with increasing the available power at the sensing node. Although spiral mapping shows a slightly better MSE performance than the proposed triangular mapping, the MSE performance of the proposed triangular mapping is still good taking into account its much lower complexity implementation.

D. Results for improving the MSE performance of the proposed mapping

1) Applying PDF-adaptive quantizer: As discussed previously in Sec. IV-A, uniform quantization is optimal for a uniformly distributed source. However, for other types of distributions, the use of non-uniform quantizers would result in a better performance. In order to verify this, we here assume that s_1 and s_2 are zero-mean Gaussian random variables with unit variance, the optimization problem of minimizing D_{tot} given in (21) subject a power constraint P is formulated and solved using CVX in order to evaluate the performance of the non-uniform quantizer. In Fig. 15, we compare the average distortion resulting from non-uniform quantization case and that of the uniform quantization (i.e., L divided equally in all regions) for a fixed power. It can be noticed that the non-uniform quantization can improve the performance of the mapping. For a fixed value of power, the adaptive quantizer achieves a better distortion compared to the case of using a uniform quantizer over the whole source range. In other words, for a given distortion, the use of a non-uniform quantizer can provide a power saving $\approx 20\%$ as can be observed from Fig. 15.

2) Exploiting temporal correlation: In order to validate the improvement achieved by the differential coding scheme in

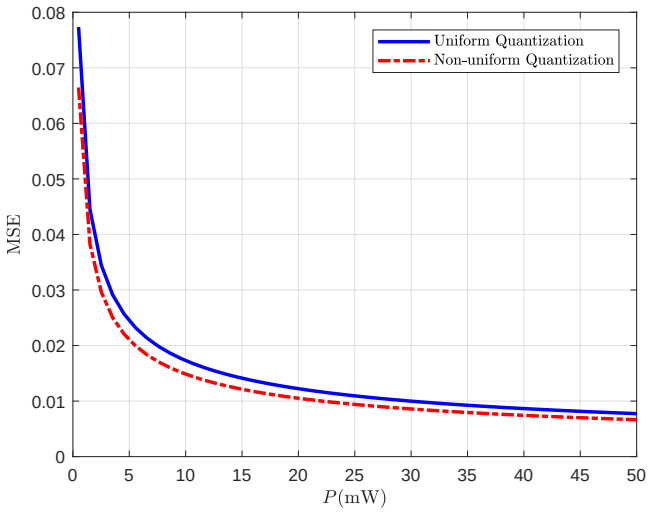

Fig. 15. Comparison of the MSE resulting from non-uniform quantization and uniform quantization vs. power.

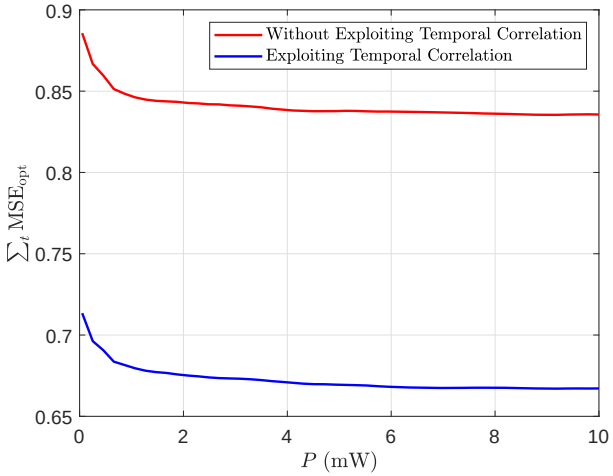

Fig. 16. Comparison of the optimized MSE with and without exploiting temporal correlation in the mapping.

Sec. IV-B1, we assume that $\sigma_w^2 = \sigma_{s_1}^2 = \sigma_{s_2}^2 = 1/12$, $\alpha = 0.7$ and $t = 3$. The total distortion over time given by (28) optimized for different values of P is plotted in Fig. 16. We observe that, for a fixed P, the use of differential coding to exploit the temporal correlation between the source signals can significantly improve the MSE performance of the proposed mapping.

3) Rotation of the mapping: In order to evaluate the effect of mapping rotation on the MSE performance in case of correlated sources, we vary the number of levels for a fixed power of $P = 5\,\mathrm{mW}$ and plot the MSE performance for different values of correlation coefficients (ρ) in Fig. 17. For each value of ρ the mapping is rotated and the MSE is calculated. It can be noticed that rotating the mapping enhances the performance of the mapping in terms of the MSE at the receiver. Moreover, one may notice that, in the case of no rotation, the MSE increases for the values of $L > 25$. This is because $L_{\mathrm{opt}} \approx 25$ for $P = 5\,\mathrm{mW}$ and $R_1 = R_2 = 1$. However, when the mapping is rotated, the ranges of s_1 and s_2 change as described in (31), and thus, the optimal of L is different (i.e., higher). It can also be concluded from Fig. 17 that the stronger correlation between the source signals the more the improvement in the MSE.

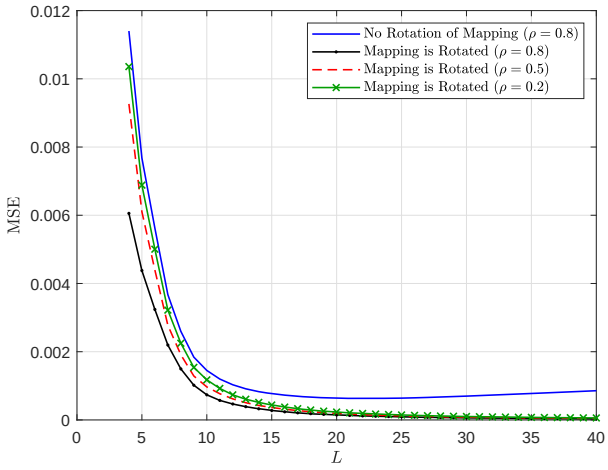

Fig. 17. Effect of the rotation of the mapping on improving the distortion error studied in terms of MSE vs. the number of levels L.

E. Results for AJSCC with Energy Scheduling Capabilities

Here, we evaluate the performance of the proposed mapping when the sensing nodes are capable of saving power and scheduling it for later use. We assume $N = 6$ time instants with no correlation existing between the source signals, $\tau = 0$ and $\sigma_n^2 = 1 \times 10^{-6}$. We let s_1 and s_2 be uniformly distributed with $R_1 = R_2 = 1$. In Fig. 18, the optimized sum MSE with and without energy scheduling are compared for different power profiles. Here, the optimized sum MSE for each case is plotted vs. the total incoming power over the whole time frame N. The considered power profiles are random, monotonically increasing, and monotonically decreasing power arrivals. It can be observed that the maximum gain from energy scheduling is obtained when the power profile is monotonically decreasing. On the other hand, in the case of a monotonically increasing power profile, there is no gain from energy scheduling because all of the power arriving at time instant i will be used with no energy scheduling for all cases. It can be deduced that the use of energy scheduling can optimize power usage for a desired distortion level.

In Fig. 19, we compare the solution of the energy scheduling problem obtained from CVX and the solution obtained using Algorithm 1 in the case of a monotonically decreasing power profile and $N = 6$. It can be observed that Algorithm 1 results in the same performance as CVX. Furthermore, the execution time[8] for both solutions is presented in Table I highlighting the fast performance of the proposed algorithm compared to CVX.

[8]Simulations are implemented in MATLAB R2017b and tested on a single CPU with an Intel Core i7 processor at 2.6 GHz, 16 GB RAM and Windows 10.

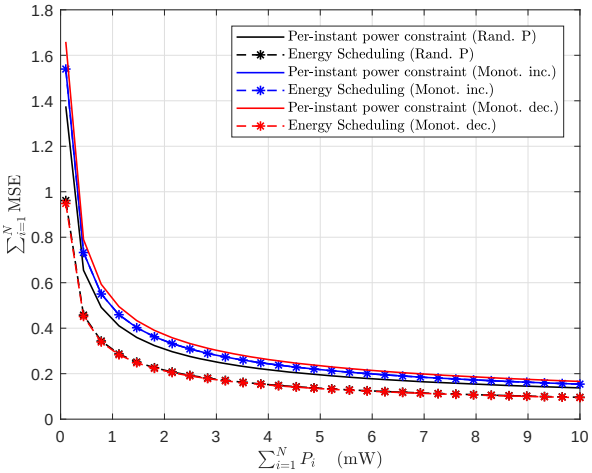

Fig. 18. Comparison of the sum MSE with per instant power constraint and energy scheduling over time $N = 6$ instants.

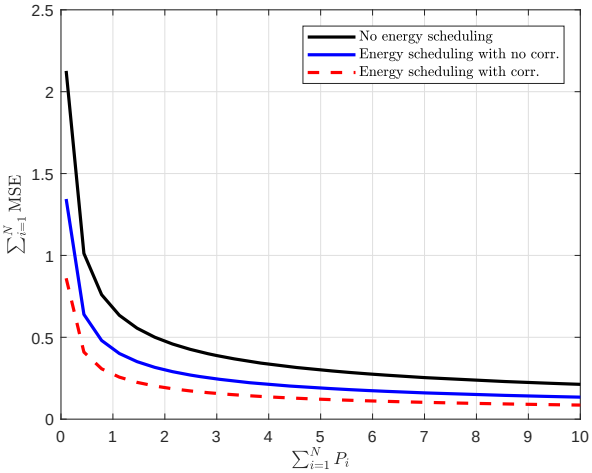

Fig. 20. Comparison of the sum MSE with and without energy scheduling over time $N = 8$ in case of correlated source signals with $\rho = 0.8$.

TABLE I
EXECUTION TIME COMPARISON FOR $N = 6$

Solver	CVX	Algorithm 1
Average execution time (s)	2.85	0.003

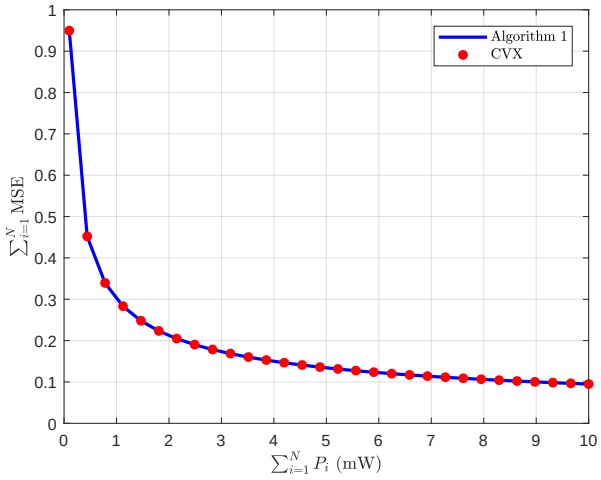

Fig. 19. Comparison of the solutions of the energy scheduling problem obtained from CVX and Algorithm. 1 for $N = 6$.

Finally, we study the improvement in the MSE performance when energy scheduling is exploited together with the existing correlation between the source signals. For that purpose, we assume that $N = 8$ and that the source signals are correlated with $\rho = 0.8$. In Fig. 20, the optimized sum MSE vs. the total incoming power is compared for the cases of no energy scheduling, exploiting energy scheduling, and exploiting energy scheduling together with correlation between sources. One can easily observe the significant improvement in the MSE performance when both energy scheduling and correlation are exploited.

VII. CONCLUSION

A low-complexity dimension reduction mapping has been proposed in this paper, namely the *triangular* mapping. The proposed mapping can be exploited in wirelessly powered sensor nodes in IoT due to its simplicity and implementability using analog circuits. Performance analysis of the proposed mapping in terms of the optimized distortion has been provided. Adaptation of the mapping to the source distribution as well as different correlations between sensor signals have been discussed and shown to improve the distortion. Moreover, the ability to schedule energy at the sensing node was shown to to improve the performance of the mapping in terms of the total distortion over time. The proposed triangular mapping in addition to the energy scheduling algorithm and the corresponding contributions of this paper form a solid base for implementing a real world wirelessly powered sensing node for IoT applications. Finding alternative compression mappings that are implementable using analog circuits is still an open area for research. Investigating optimal mappings and MSE performance bounds for non bell-shaped distributions can be studied as a future extension for the work presented in this paper. Moreover, the problem of energy scheduling in AJSCC with stochastic energy arrivals and time varying channels is appealing for future investigation.

VIII. ACKNOWLEDGMENT

The authors would like to thank Baptiste Cavarec for the fruitful discussions and constructive comments during the final stages of this work.

REFERENCES

[1] L. Chettri and R. Bera, "A comprehensive survey on internet of things (IoT) toward 5G wireless systems," *IEEE Internet of Things Journal*, vol. 7, no. 1, pp. 16–32, 2020.

[2] J. Lin, W. Yu, N. Zhang, X. Yang, H. Zhang, and W. Zhao, "A survey on internet of things: Architecture, enabling technologies, security and privacy, and applications," *IEEE Internet of Things Journal*, vol. 4, no. 5, pp. 1125–1142, 2017.

[3] A. Al-Fuqaha, M. Guizani, M. Mohammadi, M. Aledhari, and M. Ayyash, "Internet of things: A survey on enabling technologies, protocols, and applications," *IEEE Communications Surveys Tutorials*, vol. 17, no. 4, pp. 2347–2376, 2015.

[4] O. B. Akan, O. Cetinkaya, C. Koca, and M. Ozger, "Internet of hybrid energy harvesting things," *IEEE Internet of Things Journal*, vol. 5, no. 2, pp. 736–746, 2018.

[5] Y. Huang and B. Clerckx, "Large-scale multiantenna multisine wireless power transfer," *IEEE Transactions on Signal Processing*, vol. 65, no. 21, pp. 5812–5827, Nov 2017.

[6] K. W. Choi, A. A. Aziz, D. Setiawan, N. M. Tran, L. Ginting, and D. I. Kim, "Distributed wireless power transfer system for internet of things devices," *IEEE Internet of Things Journal*, vol. 5, no. 4, pp. 2657–2671, 2018.

[7] L. Xie, X. Cao, J. Xu, and R. Zhang, "UAV-enabled wireless power transfer: A tutorial overview," *IEEE Transactions on Green Communications and Networking*, pp. 1–1, 2021.

[8] P. Wu, F. Xiao, H. Huang, C. Sha, and S. Yu, "Adaptive and extensible energy supply mechanism for UAVs-aided wireless-powered internet of things," *IEEE Internet of Things Journal*, vol. 7, no. 9, pp. 9201–9213, 2020.

[9] L. Xie, J. Xu, and R. Zhang, "Throughput maximization for UAV-enabled wireless powered communication networks," *IEEE Internet of Things Journal*, vol. 6, no. 2, pp. 1690–1703, 2019.

[10] L. Wang, F. Hu, Z. Ling, and B. Wang, "Wireless information and power transfer to maximize information throughput in wban," *IEEE Internet of Things Journal*, vol. 4, no. 5, pp. 1663–1670, 2017.

[11] Z. Ling, F. Hu, L. Wang, J. Yu, and X. Liu, "Point-to-point wireless information and power transfer in wban with energy harvesting," *IEEE Access*, vol. 5, pp. 8620–8628, 2017.

[12] X. Zhao, V. Sadhu, and D. Pompili, "Low-power all-analog circuit for rectangular-type analog joint source channel coding," in *2016 IEEE International Symposium on Circuits and Systems (ISCAS)*, May 2016, pp. 1410–1413.

[13] X. Zhao, V. Sadhu, A. Yang, and D. Pompili, "Improved circuit design of analog joint source channel coding for low-power and low-complexity wireless sensors," *IEEE Sensors Journal*, vol. 18, no. 1, pp. 281–289, Jan 2018.

[14] X. Zhao, V. Sadhu, and D. Pompili, "Signal recovery performance analysis in wireless sensing with rectangular-type analog joint source-channel coding," *arxiv:2001.00131*, 2020. [Online]. Available: https://arxiv.org/abs/2001.00131

[15] X. Zhao, V. Sadhu, and D. Pompili, "Analog signal compression and multiplexing techniques for healthcare internet of things," in *2017 IEEE 14th International Conference on Mobile Ad Hoc and Sensor Systems (MASS)*, 2017, pp. 398–406.

[16] V. Sadhu, X. Zhao, and D. Pompili, "Energy-efficient analog sensing for large-scale and high-density persistent wireless monitoring," *IEEE Internet of Things Journal*, vol. 7, no. 8, pp. 6778–6786, 2020.

[17] V. Sadhu, S. Devaraj, and D. Pompili, "Towards ultra-low-power realization of analog joint source-channel coding using MOSFETs," in *2019 IEEE International Symposium on Circuits and Systems (ISCAS)*, 2019, pp. 1–5.

[18] F. Hekland, P. A. Floor, and T. A. Ramstad, "Shannon-Kotel-nikov mappings in joint source-channel coding," *IEEE Transactions on Communications*, vol. 57, no. 1, pp. 94–105, 2009.

[19] C. E. Shannon, "Communication in the presence of noise," *Proceedings of the IRE*, vol. 37, no. 1, pp. 10–21, 1949.

[20] J. A. Garcia-Naya, O. Fresnedo, F. J. Vazquez-Araujo, M. Gonzalez-Lopez, L. Castedo, and J. Garcia-Frias, "Experimental evaluation of analog joint source-channel coding in indoor environments," in *2011 IEEE International Conference on Communications (ICC)*, 2011, pp. 1–5.

[21] E. Bourtsoulatze, D. B. Kurka, and D. Gündüz, "Deep joint source-channel coding for wireless image transmission," in *ICASSP 2019 - 2019 IEEE International Conference on Acoustics, Speech and Signal Processing (ICASSP)*, 2019, pp. 4774–4778.

[22] K. Kansanen, A. N. Kim, R. Thobaben, and J. Karlsson, "Low complexity bandwidth compression mappings for sensor networks," in *2010 4th International Symposium on Communications, Control and Signal Processing (ISCCSP)*, 2010, pp. 1–5.

[23] A. Fuldseth and T. A. Ramstad, "Bandwidth compression for continuous amplitude channels based on vector approximation to a continuous subset of the source signal space," in *1997 IEEE International Conference on Acoustics, Speech, and Signal Processing*, vol. 4, 1997, pp. 3093–3096 vol.4.

[24] P. A. Floor, T. A. Ramstad, and N. Wernersson, "Power constrained channel optimized vector quantizers used for bandwidth expansion," in *2007 4th International Symposium on Wireless Communication Systems*, 2007, pp. 667–671.

[25] F. Hekland, G. E. Oien, and T. A. Ramstad, "Using 2:1 Shannon mapping for joint source-channel coding," in *Data Compression Conference*, March 2005, pp. 223–232.

[26] E. Akyol, K. Rose, and T. Ramstad, "Optimal mappings for joint source channel coding," in *2010 IEEE Information Theory Workshop on Information Theory (ITW 2010, Cairo)*, 2010, pp. 1–5.

[27] Z. Chu, F. Zhou, Z. Zhu, R. Q. Hu, and P. Xiao, "Wireless powered sensor networks for internet of things: Maximum throughput and optimal power allocation," *IEEE Internet of Things Journal*, vol. 5, no. 1, pp. 310–321, 2018.

[28] A. Gersho and R. Gray, *Vector Quantization and Signal Compression*, ser. The Springer International Series in Engineering and Computer Science. Springer US, 1991.

[29] S. Bi, Y. Zeng, and R. Zhang, "Wireless powered communication networks: an overview," *IEEE Wireless Communications*, vol. 23, no. 2, pp. 10–18, 2016.

[30] D. Tse and P. Viswanath, *Capacity of wireless channels*. Cambridge University Press, 2005, p. 166–227.

[31] Y. Hu, J. Garcia-Frias, and M. Lamarca, "Analog joint source-channel coding using non-linear curves and MMSE decoding," *IEEE Transactions on Communications*, vol. 59, no. 11, pp. 3016–3026, 2011.

[32] M. Grant and S. Boyd, "CVX: Matlab software for disciplined convex programming, version 2.1," http://cvxr.com/cvx, Mar. 2014.

[33] B. Widrow, I. Kollar, and Ming-Chang Liu, "Statistical theory of quantization," *IEEE Transactions on Instrumentation and Measurement*, vol. 45, no. 2, pp. 353–361, 1996.

[34] A. Gersho, "Quantization," *IEEE Communications Society Magazine*, vol. 15, no. 5, pp. 16–16, 1977.

[35] Bo Lu and J. Garcia-Frias, "Non-linear bandwidth reduction schemes for transmission of multivariate Gaussian sources over noisy channels," in *2012 46th Annual Conference on Information Sciences and Systems (CISS)*, 2012, pp. 1–6.

[36] P. Suárez-Casal, O. Fresnedo, and L. Castedo, "Analog transmission of spatio-temporal correlated sources over MAC with modulo mappings," *IEEE Communications Letters*, vol. 22, no. 5, pp. 1074–1077, 2018.

[37] P. Suarez-Casal, O. Fresnedo, L. Castedo, and J. Garcia-Frias, "Parametric analog mappings for correlated gaussian sources over AWGN channels," in *2016 IEEE International Conference on Acoustics, Speech and Signal Processing (ICASSP)*, 2016, pp. 3761–3765.

[38] S. Ulukus, A. Yener, E. Erkip, O. Simeone, M. Zorzi, P. Grover, and K. Huang, "Energy harvesting wireless communications: A review of recent advances," *IEEE Journal on Selected Areas in Communications*, vol. 33, no. 3, pp. 360–381, 2015.

[39] B. A. Mouris, H. Ghauch, R. Thobaben, and B. L. G. Jonsson, "Multitone signal optimization for wireless power transfer in the presence of wireless communication links," *IEEE Transactions on Wireless Communications*, vol. 19, no. 5, pp. 3575–3590, 2020.

[40] O. Ozel and S. Ulukus, "Achieving AWGN capacity under stochastic energy harvesting," *IEEE Transactions on Information Theory*, vol. 58, no. 10, pp. 6471–6483, 2012.

[41] E. Jorswieck and H. Boche, *Majorization and Matrix Monotone Functions in Wireless Communications*. Now Foundations and Trends, 2007.

[42] Kyong-Hwa Lee and D. Petersen, "Optimal linear coding for vector channels," *IEEE Transactions on Communications*, vol. 24, no. 12, pp. 1283–1290, 1976.

[43] F. Hekland, "On the design and analysis of Shannon-Kotel'nikov mappings for joint-source-channel coding," Ph.D. dissertation, Norwegian University of Science and Technology, 2007.

[44] C. Gasch and D. Brown. Data from: A field-scale sensor network data set for monitoring and modeling the spatial and temporal variation of soil moisture in a dryland agricultural field. [Online]. Available: https://doi.org/10.15482/USDA.ADC/1349683.

[45] C. K. Gasch, D. J. Brown, C. S. Campbell, D. R. Cobos, E. S. Brooks, M. Chahal, and M. Poggio, "A field-scale sensor network data set for monitoring and modeling the spatial and temporal variation of soil water content in a dryland agricultural field," *Water Resources Research*, vol. 53, no. 12, pp. 10 878–10 887, 2017.

[46] P. A. Floor and T. A. Ramstad, "Dimension reducing mappings in joint source-channel coding," in *Proceedings of the 7th Nordic Signal Processing Symposium - NORSIG 2006*, 2006, pp. 282–285.

APPENDIX

A. Proof of Lemma 1

The upper bound on p_{lc} given in (11) is obtained by assuming $s_1 \sim \mathrm{U}[0, R_1]$. Therefore, one can write

$$p_{lc}^{\text{up}} = \frac{1}{R_1}\int_0^{R_1} Q\left(\frac{\frac{d}{R_1}s_1}{\sigma_n}\right) ds_1 = \frac{1}{\sqrt{2\pi}}\frac{1}{R_1}\int_0^{R_1}\int_{\frac{d}{R_1}\frac{s_1}{\sigma_n}}^{\infty} e^{-\frac{x^2}{2}}\, dx\, ds_1. \quad (42)$$

Let $x = \frac{d}{R_1}\frac{s_1}{\sigma_n} z$. Then, we get

$$p_{lc}^{\text{up}} = \frac{1}{\sqrt{2\pi}}\frac{1}{R_1}\int_0^{R_1}\frac{d\, s_1}{R_1\sigma_n}\int_1^{\infty} e^{-\left(\frac{d}{R_1}\frac{s_1}{\sigma_n}\right)^2\cdot\frac{z^2}{2}} dz\, ds_1. \quad (43)$$

Assume $y = \frac{d}{R_1\sigma_n}s_1$. Consequently,

$$\begin{aligned} p_{lc}^{\text{up}} &= \frac{1}{\sqrt{2\pi}}\frac{\sigma_n}{d}\int_0^{\frac{d}{\sigma_n}} y\int_1^{\infty} e^{-y^2\cdot\frac{z^2}{2}} dz\, dy \\ &= \frac{1}{\sqrt{2\pi}}\frac{\sigma_n}{d}\int_1^{\infty}\int_0^{\frac{d}{\sigma_n}} y e^{-y^2\cdot\frac{z^2}{2}} dy\, dz \\ &= \frac{1}{\sqrt{2\pi}}\frac{\sigma_n}{d}\int_1^{\infty}\left(\frac{1}{z^2} - \underbrace{\frac{1}{z^2}e^{-\left(\frac{d}{\sigma_n}\right)\cdot^2\cdot z^2}}_{I}\right) dz. \end{aligned} \quad (44)$$

Integrating I by parts and substituting, one can get

$$\begin{aligned} p_{lc}^{\text{up}} &= \frac{1}{\sqrt{2\pi}}\frac{\sigma_n}{d}\left(1 - e^{-\frac{1}{2}\left(\frac{d}{\sigma_n}\right)^2} + \frac{d}{\sigma_n}\int_{\frac{d}{\sigma_n}}^{\infty} e^{-\frac{\zeta^2}{2}} d\zeta\right) \\ &= \frac{\sigma_n}{d\sqrt{2\pi}}\left(1 - e^{-\frac{1}{2}\left(\frac{d}{\sigma_n}\right)^2} + \sqrt{2\pi}\left(\frac{d}{\sigma_n}\right)Q\left(\frac{d}{\sigma_n}\right)\right). \end{aligned} \quad (45)$$

A similar expression for p_{rc}^{up} can be obtained using (10) which completes the proof.

B. Extension to $N_s : 1$ mapping

Here, we discuss the extension of our proposed triangular mapping to higher-order dimension reduction. Higher-order dimension reduction mappings were first studied in [46], in particular, 3:1, 4:1 and 3:2 extensions to the spiral mapping. However, no specific method to determine the geometry of these mappings was presented. An alternative approach was presented in [43] where cascading of two layers of 2:1 compression was used to achieve 4:1 compression. Nevertheless, the performance of the cascaded mappings was found to be worse than the direct 4:1 mapping geometry proposed in [46]. We here follow the method used in [14], [15] to extend the 2:1 rectangular mapping to $N_s : 1$ dimension reduction. The 3:1 triangular compression mapping is shown in Fig. 21 as an example. It is obtained by creating parallel planes along the z-axis, each containing a copy of the 2:1 triangular mapping. The parallel planes are separated by a distance of Δ_2. Similar, to the 2:1 case, the source point $(s_1,\ s_2,\ s_3)$ is approximated to the closest point on the curve and the accumulated length of the curve starting from the origin is transmitted. In this case, s_2 is quantized into L_1 levels and s_3 is quantized into L_2 levels (planes). The extension to $N_s : 1$ mappings can be obtained in a similar fashion where the readings of $s_i\ \forall\ i \neq 1$ are quantized while the reading of s_1 is transmitted continuously. The MSE performance at the decoder for the higher-order triangular mapping can be expressed in the same way as the higher-order rectangular mapping [14], [15] which is given by

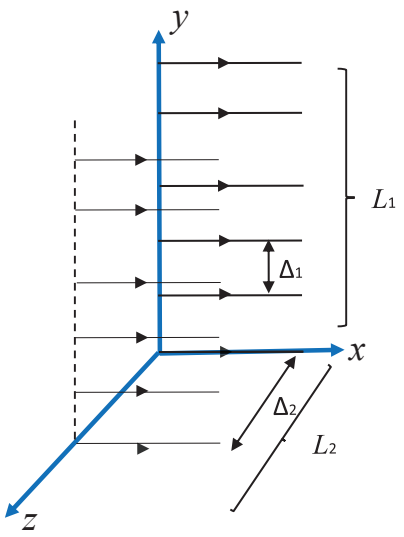

Fig. 21. Extension of the triangular mapping to 3:1 dimension reduction mapping.

$$\text{MSE}_{N_s} \approx \frac{R_1^2\prod_{j=1}^{N_s-1} L_j^2}{\gamma^2}\sigma_n^2 + \sum_{j=1}^{N_s-1}\frac{1}{12}\frac{R_{j+1}^2}{(L_j-1)^2}. \quad (46)$$

he optimal parameters of the higher-order triangular mapping are obtained in a similar way as (17) by solving the following convex optimization problem

$$\begin{aligned} &\min_{L1,\ldots,L_{N_s}} \quad (46) \\ &\text{subject to} \quad \prod_{j=1}^{N_s-1} L_j^2 d^2 \le P_{\max} \end{aligned}. \quad (47)$$

It is worth mentioning that the higher-order triangular mapping can easily be implemented by adding parallel branches similar to that of s_2 to the block diagram in Fig. 4. Moreover, the contributions of our paper, namely the techniques for improving the MSE perfomance as well as energy scheduling extend to the high-order mapping case in a straight forward fashion.